Experimental investigation of the kinematics of post-impact ice fragments

Pierrick Guegan, Ramzi Othman, Daniel Lebreton, Franck Pasco, Philippe Villedieu, Jacques Meyssonnier, Sylvie Wintenberger

▶ **To cite this version:**

Pierrick Guegan, Ramzi Othman, Daniel Lebreton, Franck Pasco, Philippe Villedieu, et al.. Experimental investigation of the kinematics of post-impact ice fragments. International Journal of Impact Engineering, 2011, 38 (10), pp.786. 10.1016/j.ijimpeng.2011.05.003 . hal-00842144

HAL Id: hal-00842144
https://hal.science/hal-00842144

Submitted on 8 Jul 2013

HAL is a multi-disciplinary open access archive for the deposit and dissemination of scientific research documents, whether they are published or not. The documents may come from teaching and research institutions in France or abroad, or from public or private research centers.

L'archive ouverte pluridisciplinaire **HAL**, est destinée au dépôt et à la diffusion de documents scientifiques de niveau recherche, publiés ou non, émanant des établissements d'enseignement et de recherche français ou étrangers, des laboratoires publics ou privés.

Accepted Manuscript

Title: Experimental investigation of the kinematics of post-impact ice fragments

Authors: Pierrick Guegan, Ramzi Othman, Daniel Lebreton, Franck Pasco, Philippe Villedieu, Jacques Meyssonnier, Sylvie Wintenberger

PII: S0734-743X(11)00080-7

DOI: 10.1016/j.ijimpeng.2011.05.003

Reference: IE 1999

To appear in: *International Journal of Impact Engineering*

Received Date: 28 June 2010

Revised Date: 19 March 2011

Accepted Date: 4 May 2011

Please cite this article as: Guegan P, Othman R, Lebreton D, Pasco F, Villedieu P, Meyssonnier J, Wintenberger S. Experimental investigation of the kinematics of post-impact ice fragments, International Journal of Impact Engineering (2011), doi: 10.1016/j.ijimpeng.2011.05.003

This is a PDF file of an unedited manuscript that has been accepted for publication. As a service to our customers we are providing this early version of the manuscript. The manuscript will undergo copyediting, typesetting, and review of the resulting proof before it is published in its final form. Please note that during the production process errors may be discovered which could affect the content, and all legal disclaimers that apply to the journal pertain.

ACCEPTED MANUSCRIPT

Experimental investigation of the kinematics of post-impact ice fragments

Pierrick Guégan[a], Ramzi Othman[a], Daniel Lebreton[a], Franck Pasco[a], Philippe Villedieu[b], Jacques Meyssonnier[c], Sylvie Wintenberger[d]

[a] *Institut de Recherche en Génie Civil et Mécanique, Ecole Centrale de Nantes, 1 Rue de la Noe BP 92101, 44321 Nantes cedex, France.*
[b] *ONERA, 2 Avenue Edouard Belin, BP 4025, 31055 Toulouse, France.*
[c] *LGGE, UMR 5183 UJF-CNRS, 54 Rue Molière, BP 96, 38402 Saint Martin d'Hères Cedex, France.*
[d] *SNECMA, Site de Villaroche, Rond Point René Ravau, Réau, 77550 Moissy Cramayel, France.*

Abstract

Hail is more hazardous for aircraft engines compared to rain and snow, mainly, because of its solid nature and high water content. In extreme cases it can lead to **engine** flame out. In order to avoid such situations, aero engines should be designed to withstand hail ingestion. For this purpose we have studied the post-impact characteristics of ice, such as particle velocity and directions of travel. To achieve this goal, a large experimental program has been undertaken, in which spherical ice specimens were projected against a rigid plate. Three specimen diameters **(6.2, 12.9 and 27.5 mm)** and four impact angles **(20, 45, 75 and 90 °)** were considered, as well as a wide range of impact velocities **(60-200 m/s)**. From this experimental work, we can conclude that the ice fragments formed after impact do not bounce back and that the post-impact ice trajectory angle is lower than 2 °. This is in line with observations found in the literature. On the other hand, the ice fragments are mainly organised in a circular cloud, when observed in the

ACCEPTED MANUSCRIPT

target plane. The center of this cloud has the same velocity as the initial ice ball tangential impact velocity. Furthermore, the cloud radius expands with a rate proportional to the ice ball normal impact velocity. Finally, each fragment inside the cloud has a relative velocity which varies linearly with its distance from the cloud center. These experimental observations should be very helpful **in developing** models and simulations of hail ingestion by aircraft engines.

Key words: Hailstorm, aircraft engines, ice fragmentation, hail ingestion.

Aircraft engines and structures can face several kind of impacts, mainly during take off and landing, such as from birds [1], tyre debris [2, 3, 4], hail [5] or sand [6, 7, 8]. These kinds of impacts can induce damage in some parts of the aircraft structure and lead eventually to **an** aircraft crash. Furthermore, impact-induced fragments can be ingested by aircraft engines and cause engine power loss. Therefore, aero engines have to satisfy safety requirements against hail ingestion to obtain certification.

Hail ingestion, as water ingestion [9, 10, 11], can cause engine power loss and in extreme cases engine flame out [12, 13, 14]. In the event of ingested hail passing through the fan into the core engine, changes in temperature, density and specific heat ratio will occur. As a result the engine will lack combustion efficiency or/and stability which can lead to its loss of thrust and eventually to a flame out. Engine manufacturers and aviation regulatory agencies have a common aim: preventing engine flame outs, roll-back or other **operational** effects that could result in an in-flight shut down when flying by stormy weather. These considerations are a major concern for the design, the certification and the **operation** of modern high bypass aircraft engines.

ACCEPTED MANUSCRIPT

The engine manufacturers need powerful numerical tools to take into account inclement weather threats in the engine design. A first model was proposed by [15]. However, to be realistic, these simulations must rely on experimental investigations of hail impact in order to understand the phenomenon, develop appropriate constitutive equations and identify the relevant parameters.

A number of references can be found in the literature about ice-impact induced damage e.g. [5, 16, 17], fatigue induced damage e.g. [16] or high velocity ice impacts on composite panels e.g. [5, 17]. On the other hand, low velocity ice impacts, i.e., for velocities lower than $10\,\mathrm{m.s^{-1}}$, were investigated in Refs. [18, 19, 20, 21, 22, 23]. These latter works aimed at defining the transition between the rebound and fragmentation regimes.

In order to understand hail ingestion by aircraft engines, Pan, Render et al. [24, 25, 27, 26, 28, 29, 30] have studied the impact fragmentation characteristics of hailstones on rigid targets. They were interested in post-impact particle size, particle velocity and travel directions. In Ref. [26] a patternator technique was used. A still photography technique was also employed in Ref. [25, 28]. These investigations were extended to study the effect of target curvature [29] and target rotation [27]. Subsequently, the methodology was applied to consider the hail mass distribution behind a rotating fan and spinner assembly [30]. Pan, Render et al. [24, 25, 27, 26, 28, 29, 30] have shown that the Rosin-Rammler [31] distribution, also called Weibull distribution [32], which is also used in rock fragmentation [33], is well suited to represent the particle size and particle velocity distributions.

In the present paper, we investigate the kinematics of post-impact ice

ACCEPTED MANUSCRIPT

fragments. Render and Pan [26] have observed that the fragments do not bounce back, i.e., the post-impact angles are very low with the fragments trajectories remaining almost in the plane of the target. This result was obtained by a patternator technique. One aim of the present work is to check this result against high speed photography observations. On the other hand, the fact that the particle velocity distribution was found by [28] to be of the Rosin-Rammler [31] type is not enough to describe the fragments movement completely. Indeed, the distribution only indicates what percentage of mass fragments moves at a given velocity. In the present work, we are also interested in obtaining a better description of the kinematics of fragments in the plane of the target. To this aim a wide experimental program was carried out to assess the influences of the ice projectile diameter, impact angle and impact velocity.

1. Method

1.1. Ice preparation

The ice spherical specimens were prepared using moulds made of two hollow half-spheres in order to facilitate the removal of the ice ball. The moulds were filled with cooled water (between 4 and 8 °C), then placed in a freezer (between -25 and -18 °C). Subsequently, the ice balls were removed from the moulds after 24 hours and kept in the freezer until the beginning of the test.

Hailstones can have diameters ranging from 2 to 100 mm [26]. In the present study, three diameters (D_0) were considered: 6.2, 12.9 and 27,5 mm corresponding to a mass of approximately 0.1, 1 and 10 g, respectively. It

ACCEPTED MANUSCRIPT

must be noted that since the tests were performed at room temperature melting can induce important dimension inaccuracies in the ice of which diameter is lower than 6 mm. On the other hand, it is hard to analyse images of projectiles with large diameters because of the huge number of fragments formed. Note that Pan and Render [26, 28] worked mainly with ice balls 12.7 mm in diameter.

1.2. Experimental set-up

The experimental set-up consists of a gas gun, that comprises a high pressure chamber, a cooled chamber and a tube, a target plate and the instrumentation (Figure 1). The high pressure chamber works with nitrogen gas and can go up to 85 bar (8.5 MPa). The actual applied pressures were between 0.6 and 3.9 bar (0.06 and 0.39 MPa), which results in impact velocities (V_0) ranging between 60 and 200 $\mathrm{m.s^{-1}}$. This velocity range corresponds to that of a low engine power regime, such as during aircraft descent. It is in this regime that inclement weather effects are mostly encountered [14]. It is worth noticing that Pan and Render [26, 28] were limited to impact velocities in the range 100 to 175 $\mathrm{m.s^{-1}}$.

The cooled chamber is made out of stainless steel. It is located between the high pressure chamber and the gas tube. Its role is to house the ice projectile while preventing it from melting before the strike. It is cooled by the flow of an antifreeze - water mixture maintained at a temperature between -4 and 0 °C by a cooling generator. The cooled chamber is connected to the canon made out of a stainless **steel** tube. The cooled chamber inner dimensions and the tube inner diameter are adapted to the ice ball diameters, so that no sabot is needed. Since we performed our tests with three ice ball

ACCEPTED MANUSCRIPT

diameters, three different cooled chambers and three different tubes were used.

The target is a glass plate ($200 \times 200\,\mathrm{mm}^2$) 20 mm in thickness. The choice of glass as the target material was motivated by two reasons. Firstly, glass has a stiffness comparable to some metallic material such as aluminium (its Young's modulus is about 64 GPa). Secondly, since glass is transparent, it is possible to use back-lighting which yields more homogeneous light on the target than front-lighting.

This target is mounted on a bearing system allowing two degrees of freedom (Figure 2): a translation along the vertical direction and a rotation around the horizontal axis perpendicular to the (horizontal) gas tube thus allowing changes in the impact angle α. The impact angle is defined as the angle between the projectile trajectory before impact and the normal to the plane of the target. In the present work, four values of the impact angle α were considered: 20, 45, 67 and 90 °.

The experimental set-up is instrumented by two laser barriers to measure the ice ball impact velocity. Furthermore, two high speed video cameras were used in order to record the post-impact characteristics. The first camera was used to film the lateral side, i.e., the plane perpendicular to the target that contains the gas-tube axis, whereas the second camera was used to film the front side, i.e., the target surface. The two cameras were synchronised. The trigger was given by the first laser barrier. The adopted acquisition frequency of the cameras was 15000 frames per second.

The initial conditions of all our tests are given in Table 1.

ACCEPTED MANUSCRIPT

2. Results

2.1. General observations

Figures 3 and 4 show the sequences of images for an ice ball fragmentation obtained with the front camera and the lateral camera, respectively. In this test, the ice ball diameter, impact angle and impact velocity were 12.9 mm, 20 °and 120.8 m.s^{-1}, respectively (Test No. 15). Both cameras were synchronised and took 15000 frame per second, so that, for example, photographs (a) on Figures 3 and 4 were taken at the same time. The resolutions of the front and lateral camera were 320 × 832 pix^2 and 1024 × 128 pix^2, respectively. Figures 3(a) and 4(a) show the ice specimen just before impact. The first contact between the ice ball and the plate is shown in Figures 3(b) and 4(b). Fragmentation begins at Figures 3(c) and 4(c).

From Figures 3 and 4, we can divide the fragmentation process into two stages. In a first stage, only the front part of the ice ball fragments (Figure 3(c) to (e) and Figure 4(c) to (e)). The created fragments are ejected first and form a low density chaotic cloud. In a second stage, the remaining ice projectile collapses (Figure 3(f) to (l) and Figure 4(f) to (l)) yielding a high density, almost circular, cloud. We can also notice from Figure 4 that the post-impact angle, which we define as the angle between the fragments trajectories and the plane of the target, is very low. Fragments trajectories lie almost in the target plane.

The above observations are also confirmed in Figure 5 where photos (a) to (f) show images of ice fragmentation for a normal impact at a velocity of 150.4 m.s^{-1}. The two photos in Figure 6, which are magnifications of Figures 5(b) and 5(e), show that the first ejected particles which make the low density

ACCEPTED MANUSCRIPT

cloud have a high velocity, higher than the initial ice ball impact velocity. **This is consistent with results of Render and Pan [26] who observed also that particles formed immediately after impact moves greatly faster than the approaching ice ball velocity.** Figure 6(a) shows two particles with a post-impact velocities of $335\,\mathrm{m.s^{-1}}$and $443\,\mathrm{m.s^{-1}}$, respectively, to be compared to the ice ball impact velocity of $150.4\,\mathrm{m.s^{-1}}$. On the other hand, the fragments created during the second stage, that form the high density cloud, have lower velocities. As an illustration Figure 6(b) shows two particles, one with a post-impact velocity of $52\,\mathrm{m.s^{-1}}$and the other with a post-impact velocity of $18\,\mathrm{m.s^{-1}}$. The difference in the post-impact velocities can be explained as follows. At the beginning of the impact, the ice ball has a high initial velocity and elastic energy is stored in the yet unfragmented material. Only a small ratio of the mass is fragmented. Particles are ejected with a high velocity, which can be even higher than the nominal impact-velocity owing to the energy release. Furthermore, as the first stage cloud has a low density of fragments, the likelihood that collisions occur is low. As the second stage of the fragmentation process begins, the remaining unfragmented ice mass has already lost a part of its kinetic energy during the first stage. In addition, the second stage cloud of fragments has a higher density. Hence, multiple collisions happen that consume part of the kinetic energy of the particles.

It is worth to point out here that the post-impact particles velocities were determined by measuring the particles coordinates (in pixels) in several consecutive images. **This particle tracking is processed manually. In order to have a full comprehension of the post-impact fragment**

ACCEPTED MANUSCRIPT

kinematics, the tracking is operated on the center of the high density cloud and its circular counter and also on three to seven particles inside the cloud. The velocities were first determined in pix.s^{-1} then converted to m.s^{-1}from the calibration coefficient determined from a calibration image **which corresponds to a mellimetric grid. Considering, the camera settings, the accuracy of displacement measurements are at best 0.01 pix and at worst 0.1 pix**.

2.2. Kinematics in the normal plane

In this section, we are mainly interested in the fragments post-impact angle. The ice ball impact angle α and fragments post-impact angle γ are represented in Figure 7. The angle γ is defined as the maximum angle between the fragments trajectories and the plane of the target. This angle is determined from the lateral camera images as shown in Figure 8. Figure 9 shows the different values of post-impact angles obtained for all the experiments. It seems that the post-impact angle γ is independent of the ice ball impact velocity V_0, of the impact angle α and of the projectile diameter D_0. All the measured values of γ lie in the range between 1 and 2 °. Therefore, the normal velocity of fragments can be considered as negligible with respect to their tangential velocity, that is, the fragments kinematics is governed by their sole tangential velocity **which is in line with the findings of Render & Pan [26] who observed a low bounce normal to the surface of the ice ball fragments**.

ACCEPTED MANUSCRIPT

2.3. Kinematics in the target plane

As explained in section 2.1, the fragmentation process is divided into two stages. The first stage yields a low density, high velocity, chaotic cloud of fragments. The second stage is characterized by a high density, low velocity, circular cloud. In this section, we focus on the kinematics of the fragments created during the second stage. Mainly, we are interested in the velocity of the cloud center, the rate of surface expansion of the cloud and in the velocities of fragments relative to a (moving) reference point in the moving cloud. To this aim we analyse the images obtained by using the front camera (Figure 10). For each image i, the contour of the second-stage cloud of fragments is approximated by a circle of center C_i and radius R_i. By analysing the sequence of images for each test, we can obtain the evolution with time of the cloud center and radius.

Figure 11 shows the schematic of the superposition of two cloud contours, one corresponding to the instant when the specimen hits the target ("first-contact" time; corresponding image i_0), the other at a post-impact time (image i). Note that the "initial" cloud, represented as a circle, should in fact be the elliptical projection of the undamaged spherical specimen onto the target plane (along its trajectory before impact). The y axis corresponds to the projection of the trajectory of the ice ball before impact on the plane of the target. The origin of coordinates is taken at the center C_{i_0} of the initial cloud, so that $x_{i_0} = y_{i_0} = 0$. Our analyse of the different tests has shown that the contours centers remain aligned with the y axis (i.e., in the same vertical plane that contains the ice ball trajectory before impact) (see Figure 12). In other words, for any image i, the center of the fragments cloud

ACCEPTED MANUSCRIPT

is such that $x_i = 0$, and is thus defined only by y_i.

2.3.1. Velocity of the cloud center

Figure 13 is a plot of the positions of the centers C_i, defined by the coordinate y_i, as function of time. This figure corresponds to a test performed with an ice ball of diameter $D_0 = 12.9\,\mathrm{mm}$, an impact angle $\alpha = 67.2\,^\circ$and an impact velocity $V_0 = 118.8\,\mathrm{m.s^{-1}}$(Test No. 24). The variation of y_i versus time is almost linear and can be approximated by

$$y(t) = at + b, \tag{1}$$

where a and b are two constants. In the case shown in Figure 13, $a = 42.05\,\mathrm{m.s^{-1}}$and $b = -111.9\,\mathrm{mm}$. a is the velocity of the cloud center in the target plane, i.e., the tangential velocity of the cloud center, which is denoted by V_{C_t} in the following. It is worth to compare V_{C_t} to the ice ball tangential impact velocity V_{0_t} which is such as

$$V_{0_t} = V_0 \cos\alpha, \tag{2}$$

where V_0 and α are the ice ball impact velocity and impact angle, respectively. In the case shown in Figure 13, the impact velocity V_0 is $118.8\,\mathrm{m.s^{-1}}$and the tangential impact velocity V_{0_t} equals $46.04\,\mathrm{m.s^{-1}}$. Hence, the ratio V_{C_t}/V_{0_t} is equal to 0.91. This means that the tangential velocity of the cloud center is of the same order of magnitude **as** the normal impact velocity. In order to confirm this conclusion, we have plotted the ratio V_{C_t}/V_{0_t} for the all the experiments in Figure 14(a). The values of the ratio V_{C_t}/V_{0_t} are mostly between 0.9 and 1.1. In order to reduce the effect of experimental noise we have computed the average value for each experimental configuration (see

ACCEPTED MANUSCRIPT

Figure 14(b)). This figure shows that V_{C_t}/V_{0_t} is independent of the diameter D_0 and of the impact angle α. **Nevertheless, more scatter is obtained with results of $D_0 = 6.2$ mm than those of $D_0 = 12.9$ and 27.5 mm. Indeed, the geometry of low-diameter ice balls is more sensitive to melting than the geometry of balls with important diameters. More precisely, melting can affect the spheric and smooth shape of ice balls with low diameter. As the scatter in results is lower than 10%, we conclude that melting has an insignificant effect on V_{C_t}/V_{0_t} ratio. Namely, the average ratio V_{C_t}/V_{0_t} is between 0.96 and 1.01, except for two configurations, ($D_0 = 6.2$ mm; $\alpha = 45\,^\circ$) and ($D_0 = 27.5$ mm; $\alpha = 67\,^\circ$). As the average value for all experiments is 0.986, we can state** that the tangential velocity of the cloud center V_{C_t} is almost equal to the ice ball tangential impact velocity V_{0_t}. Then we can assume that

$$V_{C_t} \approx V_{0_t}. \tag{3}$$

2.3.2. Surface expansion rate of the fragments cloud

The surface expansion rate of the cloud of fragments is characterised by the rate of expansion of the cloud radius. For each test we study the variation of the circular cloud radius versus time. This variation is almost linear and can be approximated by

$$R(t) = V_R t + R_0, \tag{4}$$

where $R_0 = D_0/2$ is the initial radius of the ice ball and $V_R = \dot{R}$ is the radius expansion rate.

Figure 15(a) shows the values of V_R for the all our experiments as a function of the ice ball normal impact velocity V_{0_n}. V_{0_n} is the component of

ACCEPTED MANUSCRIPT

the ice ball impact velocity normal to the target plane:

$$V_{0_n} = V_0 \sin(\alpha). \tag{5}$$

Figure 15(a) shows that the radius expansion rate increases with increasing normal impact velocity. Quantitatively, the radius expansion rate can be approximated by the linear relation

$$V_R \approx K_n V_{0_n}, \tag{6}$$

where K_n is a constant. From Figure 15(a), $K_n \approx 0.585$.

The ratios $K_n = V_R/V_{0_n}$ for the different experiments are plotted in Figure 15(b). It seems that K_n is independent of the test configuration: there is no special tendency neither as a function of the ice ball diameter nor of the impact angle. This is also confirmed by Figure 15(c) where the average value for each configuration is represented. **Moreover, we compare the values of K_n obtained with tests of similar conditions in Table 2. More precisely, we compare K_n of Tests 14 and 15 (D_0 = 12.9 mm, α =20°, $V_0 \approx$ 120 m/s), 17 and 18 (D_0 = 12.9 mm, α =20°, $V_0 \approx$ 158.5 m/s) and 19 and 20 (D_0 = 12.9 mm, α =45°, $V_0 \approx$ 158 m/s). It comes that the difference of the two values of K_n obtained by two tests in the same configuration is around 10%. Hence, we can confirm that K_n is independent of the test configuration and that the scatter observed in the values of K_n are rather due to eperimental inaccuracies and not to a more complex behaviour of the fragmentation process.**

ACCEPTED MANUSCRIPT

2.3.3. Fragments relative velocities

In sections 2.3.1 and 2.3.2, we have derived relations for the fragments center velocity and fragments cloud radius rate, respectively. In other words we can describe the velocity of the fragments near the center of the cloud and at its boundary. In the section, we are interested in the velocity of fragments inside the cloud. This velocity is studied in the mobile reference frame, i.e., we measure the velocity relative to the center of the cloud (Figure 16).

First, it is observed that the relative velocity of fragments V_r at a distance r from the center is dependent only on this distance:

$$\vec{V_r} \equiv \vec{V_r}(r). \tag{7}$$

Second, the relative velocity is along the radius line, i.e.,

$$\vec{V_r}(r) = V_r(r)\vec{\mathrm{e}}_r, \tag{8}$$

where $\vec{\mathrm{e}}_r$ is defined in Figure 16.

The variation of V_r in terms of the distance r is represented in Figure 17 for different experimental configurations. It comes from this figure that the velocity V_r increases with r, which explains the cloud expansion. The fragments near the center move slower than that at the boundary. Moreover, the variation of of V_r versus r can also be approximated by a linear relation

$$\vec{V_r}(r) \approx \nu r, \tag{9}$$

where ν is a constant which can be determined by considering the radius expansion rate V_R. Indeed, the velocity of fragments at the boundaries $V_r(R)$ should be equal to radius expansion rate V_R, so that the relative velocity of

ACCEPTED MANUSCRIPT

a fragment inside the cloud can be expressed as

$$\vec{V}_r(r) \approx V_R \frac{r}{R}. \tag{10}$$

3. Discussion

Despite the large experimental program undertaken, several possibly influencing parameters were neglected in this study, for example the temperatures of the ice ball and of the target.

Temperature influence several mechanical properties. Hence, there is no reason to neglect its effect on the ice fragmentation process. However, natural hail temperatures are generally between -60 °C and 0 °C. This is a rather narrow temperature range. In this work, we have considered ice balls at about -20 °C, which is not far from the middle of the temperature range. Therefore, we think that the experimental results obtained at this temperature are representative of what can happen over the total range, i.e., $[-60 - 0]$ °C.

Concerning the target temperature, the problem is slightly different as the target was at room temperature in our study. However, Render and Pan [26] worked at two temperatures (room temperature and -14 °C) and they showed that the target temperature does not induce significant changes in the results.

Several other parameters such as the projectile micro-structure and the target surface roughness might influence the fragmentation process and the kinematics of fragments . In our case, the influence of the micro-structure was not considered. However, we prepared the ice projectiles following the same procedure in order to ensure the same micro-structure.

ACCEPTED MANUSCRIPT

We think that the observed tendencies on the fragments kinematics should be also observed when changing some parameters as concerns the ice ball or the target. However, the constants determined here would not be the same. Therefore, the value of constant K_n (Eq. 6) might change if we change the ice micro-structure or the target material for example. Moreover, Eq. (3), giving the cloud center velocity, can be more generally expressed as

$$V_{\mathrm{C}_t} \approx K_t V_{0_t}, \tag{11}$$

where K_t is a constant that possibly depends on the target roughness. We think it reasonable that for smooth surfaces, which is the case with our glass target, K_t tends toward 1. However, K_t could be significantly less than 1 for rough surfaces.

4. Conclusion

The kinematics of the ice fragmentation process was investigated experimentally. We have observed that the post-impact angle is lower than 2 °, which confirms the observations reported in the literature. On the other hand, we have observed that the ice fragments are mainly organised in a circular cloud in the target plane. The center of this cloud has the same velocity as the tangential component of the projectile velocity and the cloud radius expands with a rate proportional to the projectile normal velocity. Moreover, fragments inside the cloud have a relative velocity with respect to the cloud center which varies linearly with their distance from this center. We think that these experimental results give valuable information about the ice fragmentation process, which can help modelling and simulating hail ingestion by aircraft engines.

ACCEPTED MANUSCRIPT

5. Acknowledgements

This work was carried out in the framework of the SIMICE program (No. 07 TLOG 20) of the National Research Agency (Agence Nationale de la Recherche - ANR). This agency is highly acknowledged for its financial support. Authors would also like to thank Snecma for its industrial support as coordinator of this program.

References

[1] Yulong L., Yongkang Z., Pu X., 2008. Study of Similarity Law for Bird Impact on Structure. Chinese J. Aeronautics, 21:512–517.

[2] Mines, R.A.W., McKown, S., Birch, R.S., 2007. Impact of aircraft rubber tyre fragments on aluminium alloy plates: I-Experimental. Int. J. Impact Eng., 34:627–646.

[3] Karagiozova, D., Mines, R.A.W., 2007. Impact of aircraft rubber tyre fragments on aluminium alloy plates: II-Numerical simulation using LS-DYNA. Int. J. Impact Eng. 34:647–667.

[4] Guégan P., Othman R., LeBreton D., Pasco P., Swiergiel, N., Thevenet P., 2010. Experimental investigation of rubber ball impacts on aluminium plates. Int. J. Crashworthiness, accepted.

[5] Kim, H., Welch, D.A., Kedward, K.T., 2003. Experimental investigation of high velocity ice impacts on woven carbon/epoxy composite panels. Compos. Part A, 34:25–41.

ACCEPTED MANUSCRIPT

[6] Grant, G., Tabakoff, W., 1975. Erosion prediction in turbo-machinery resulting from environment solid particles. J. Aircraft, 12:471–478.

[7] Tabakoff, W., Malak, M.F., Hamed, A., 1987. Laser measurement of solid-particle rebound parameters impinging on 2024 aluminium and 6A1-4V titanium alloys. AIAA J., 25:721–726.

[8] Tan, S.C., Harris, P.K., Elder, R.L., 1994. A unique test facility to measure particle restitution and fragmentation. International gas turbine and aeroengine congress and exposition, 94-GT-350, Hague, Netherlands, June 1994.

[9] Povarov, O., Rastorguev, V., Bodrov, A., 1986. Interaction of a drop with solid surface. Power Eng., 24:151–155.

[10] Papadakis, M., Breer, M., Craig, N.C., Bidwell, C.S., 1991. Experimental water droplet impingement data on modern aircraft surfaces. AIAA paper 91–0445.

[11] Murthy, S.N.B., 1991. Transient performance of fan engine with water ingestion. AIAA paper 91–1897.

[12] Aerospace Industries Association, 1989, PC338-1 Project report, Investigation of engine power loss and instability in inclement weather.

[13] AGARD Report AR-332, september 1995.

[14] Define, K., 1990. Inclement wheather induced aircraft engine power loss. AIAA paper 90–2169.

ACCEPTED MANUSCRIPT

[15] Gopalaswamy, N., Murthy, S.N.B., 1994. Massive particle ingestion in engine inlet. AIAA paper 94–0364.

[16] Mahinfalah, M., Skordahl, R.A., 1998. The effects of hail damage on the fatigue strength of a graphite/epoxy composite laminate. Compos. Struct., 42:101–106.

[17] Park, H., Kim, H., 2009. Damage resistance of single lap adhesive composite joints by transverse ice impact. Int. J. Impact Eng., in press, doi:10.1016/j.ijimpeng.2009.08.005

[18] Araoka, K., Maeno, N., 1978. Measurement of the restitution coefficients of ice. Low Temp. Sci. Ser. A,36:55–65. (in Japanese with English summary)

[19] Bridges, F.G., Hatzes, A.P., Lin, D.N.C., 1984. Structure, stability and evolution of Saturn's rings. Nature, 309:333–335.

[20] Hatzes, A.P., Bridges, F.G., Lin, D.N.C., 1988. Collisional properties of ice spheres at low impact velocities. Mon. Not. R. Astron. Soc., 231:1091–1115.

[21] Higa, M., Arakawa, M., Maeno, N., 1996. Measurements of restitution coefficients of ice at low temperatures. Planet. Space Sci., 44:917–925.

[22] Higa, M., Arakawa, M., Maeno, N., 1998. Size dependence of restitution coefficients of ice in relation to collision strength. Icarus, 133:310–320.

[23] Guégan, P., Othman, R., Lebreton, D., Pasco, F., Villedieu, P.,

ACCEPTED MANUSCRIPT

404 Meyssonnier, J., Wintenberger,S., 2010. Critical impact velocity for ice
405 fragmentation. Cold Reg. Sci. Technol., submitted.

406 [24] Render, P.M., Pan, H., Sherwood, M., Riley, S.J., 1993. Studies into the
407 ingestion characteristics of turbofan engines. AIAA paper 93–2174.

408 [25] Pan, H., Render, P.M., 1994. Experimental studies into the hail ingestion
409 of turbofan engines. AIAA paper 94-2956.

410 [26] Render, P.M., Pan, H., 1995. Experimental studies into hail impact
411 characteristics. J. Propuls. Power, 11:1224–1230.

412 [27] Pan, H., Render, P.M., 1995. The influence of target rotation on impact
413 characteristics of simulated hailstones. AIAA paper 95–3038.

414 [28] Pan, H., Render, P.M., 1996. Impact characteristics of hailstones simu-
415 lating ingestion by turbofan aeroengines. J. Propuls. Power, 12:457–462.

416 [29] Pan, H., Render, P.M., 1997. Effect of target curvature on the impact
417 characteristics of simulated hailstones. J. Aero. Eng., 211:81–90.

418 [30] Pan, H., Render, P.M., 1998. Studies into hail ingestion of turban en-
419 gines using a rotating fan and spinner assembly. Aeronautical J., 102:45–
420 51.

421 [31] Rosin, P., Rammler, E., 1933. The laws governing the fitness of powdered
422 coal. J. Inst Fuel, 7:29–36.

423 [32] Tuhkuri, J., 1994. Analysis of ice fragmentation process from measured
424 particle size distribution of crushed ice. Cold Reg. Sci. Technol., 23:69–
425 82.

ACCEPTED MANUSCRIPT

[33] Hamdi, E., du Mouza, J., 2005. A methodology for rock mass calibration and classification to improve blast results. Int. J. Rock Mech. Min. Sci., 42:177–194.

ACCEPTED MANUSCRIPT

ACCEPTED MANUSCRIPT

6. Figures and tables

ACCEPTED MANUSCRIPT

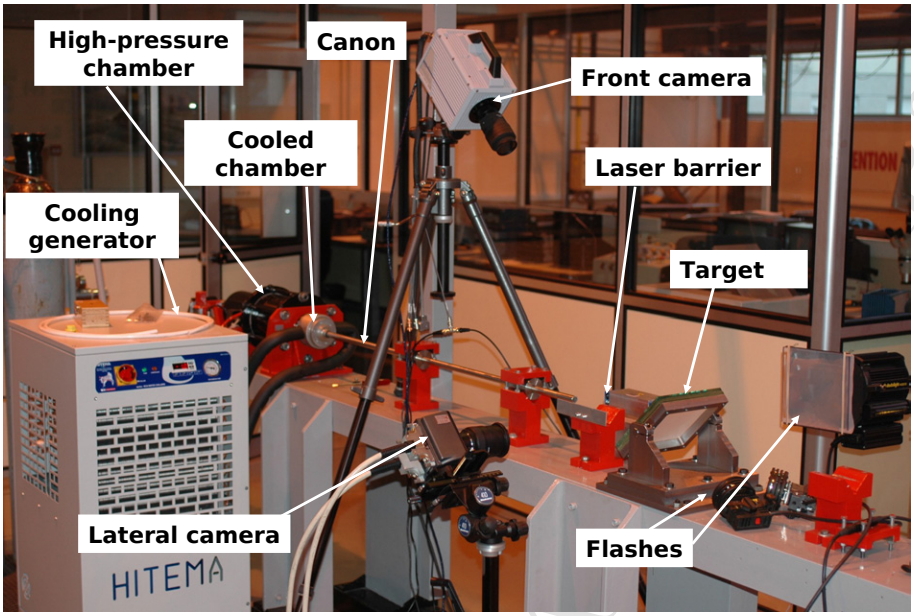

Figure 1: Overview of the experimental setup.

ACCEPTED MANUSCRIPT

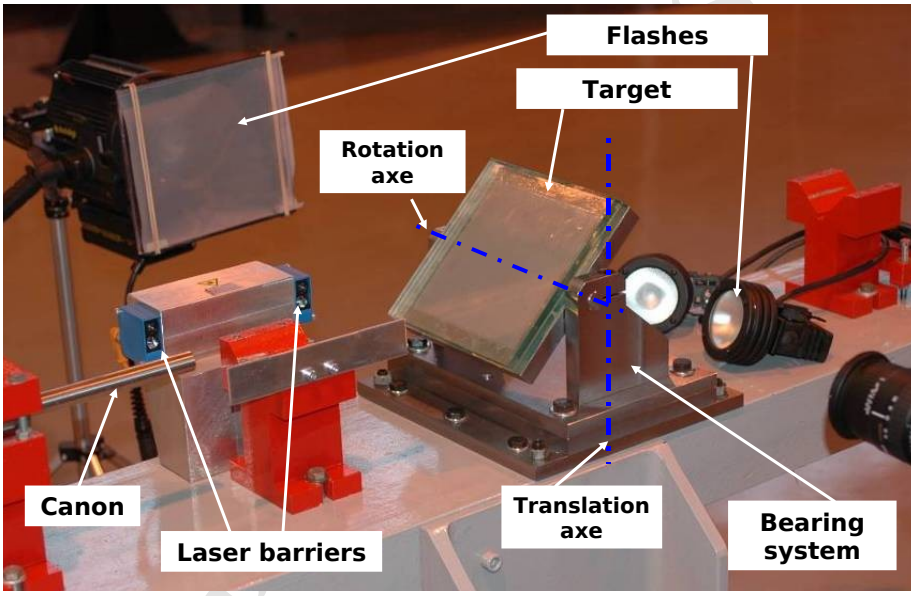

Figure 2: Overview of the target and its bearing system.

ACCEPTED MANUSCRIPT

ACCEPTED MANUSCRIPT

Test No.	D_0 (mm)	$\alpha(^\circ)$	V_0 (m.s^{-1})
1	6.2	20	135.8
2	6.2	20	163.2
3	6.2	20	117.1
4	6.2	45	185.7
5	6.2	45	138.0
6	6.2	45	141.9
7	6.2	67	174.9
8	6.2	67	121.9
9	6.2	67	105.2
10	6.2	90	131.0
11	6.2	90	152.7
12	6.2	90	97.2
13	6.2	90	202.8
14	12.9	20	119.9
15	12.9	20	120.8
16	12.9	20	112.1
17	12.9	20	159.4
18	12.9	20	157.9
19	12.9	45	158.0
20	12.9	45	157.9
21	12.9	45	164.8
22	12.9	45	120.3
23	12.9	45	116.4
24	12.9	67.2	118.8
25	12.9	67.2	91.1
26	12.9	67.2	130.5
27	12.9	67.2	155.2
28	12.9	90	122.2
29	12.9	90	114.7
30	12.9	90	146.5
31	12.9	90	150.4
32	27.5	20	66.8
33	27.5	20	97.4
34	27.5	20	116.4
35	27.5	45	66.1
36	27.5	45	98.2
37	27.5	45	116.2
38	27.5	67.2	60.5
39	27.5	67.2	100.0
40	27.5	67.2	116.1
41	27.5	90	66.1
42	27.5	90	97.0
43	27.5	90	113.9

Table 1: Entry parameters of the impact tests

Test No.	D_0 (mm)	$\alpha(^\circ)$	V_0 ($\mathrm{m.s^{-1}}$)	K_n
14	12.9	20	119.9	0.716
15	12.9	20	120.8	0.650
17	12.9	20	159.4	0.526
18	12.9	20	157.9	0.574
19	12.9	45	158.0	0.565
20	12.9	45	157.9	0.510

Table 2: Values of K_n for some tests.

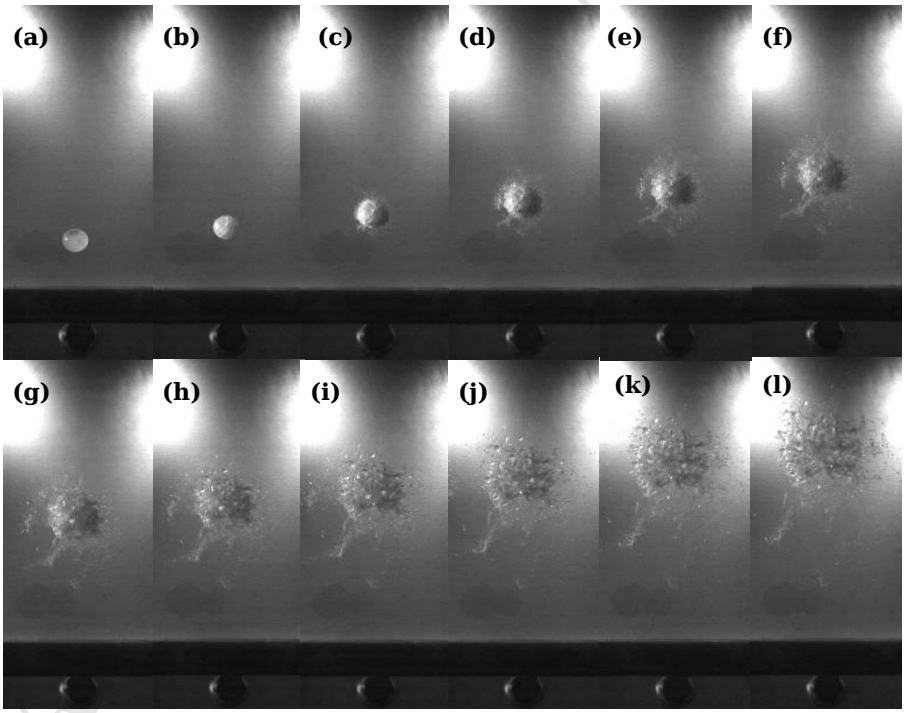

Figure 3: Image sequence of the ice ball fragmentation taken by the front camera (diameter: 12.9 mm, impact angle 20 °, impact velocity: 120.8 $\mathrm{m.s^{-1}}$).

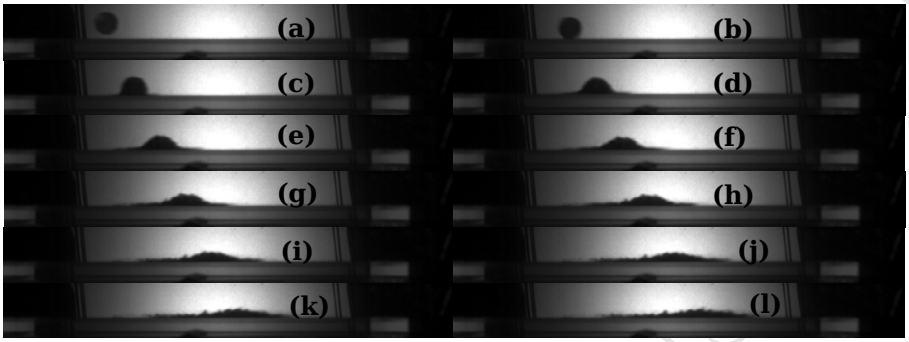

Figure 4: Image sequence of the ice ball fragmentation taken by the lateral camera (diameter: 12.9 mm, impact angle 20 °, impact velocity: 120.8 m.s^{-1}).

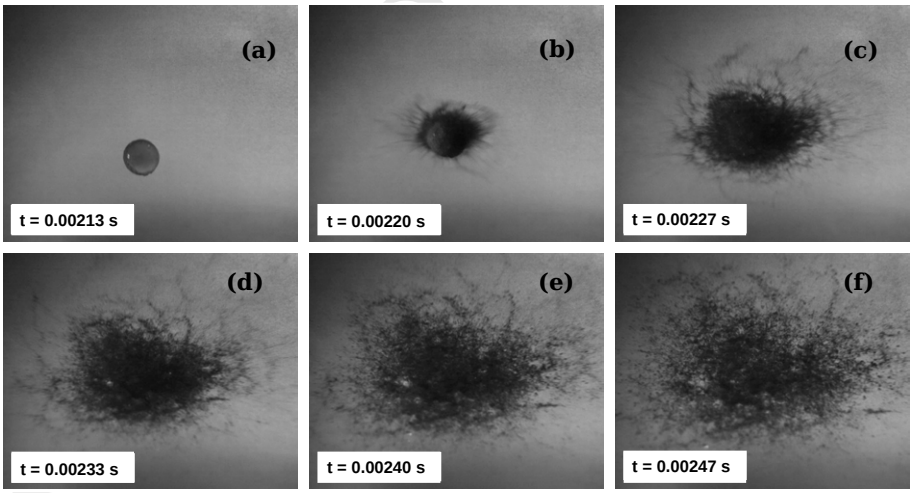

Figure 5: Front view of ice fragmentation (diameter: 12.9 mm, impact angle 90 °, impact velocity: 150.4 m.s^{-1})).

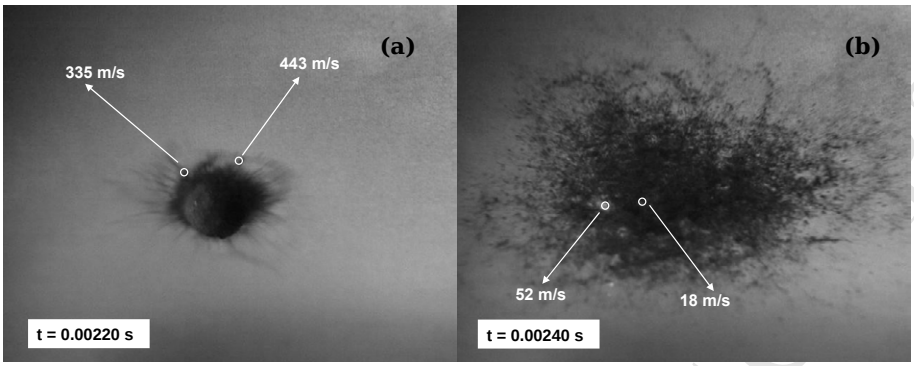

Figure 6: Magnification of the areas shown in Figure 5(b) and Figure 5(e).

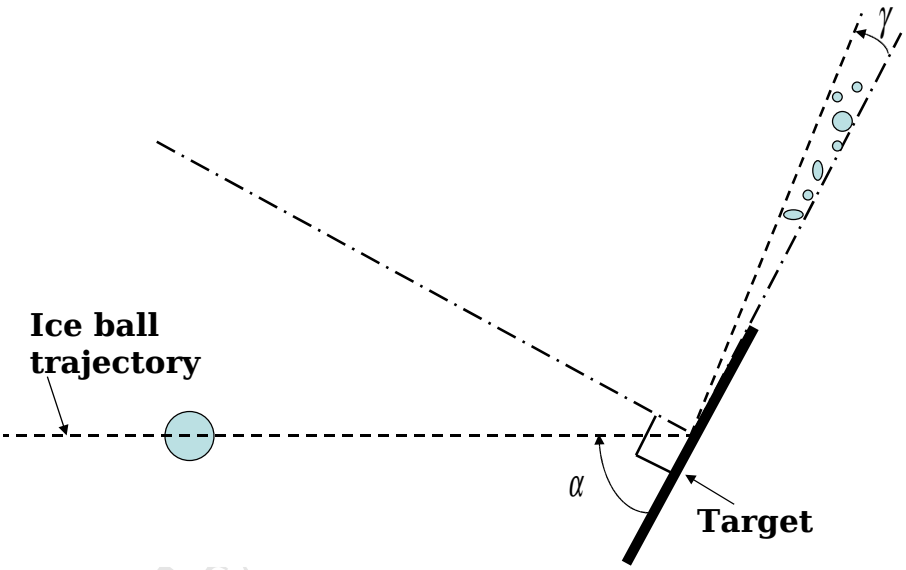

Figure 7: Definition of the post-impact angle.

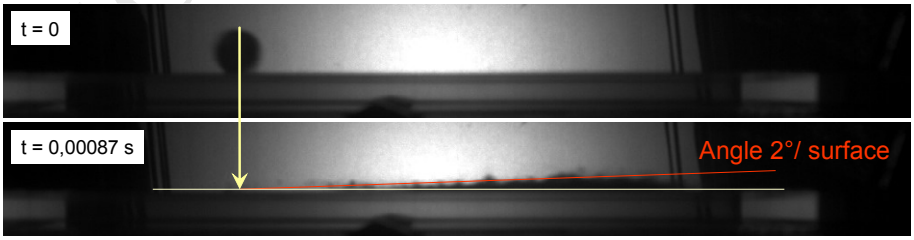

Figure 8: Example of measurement of the post-impact angle.

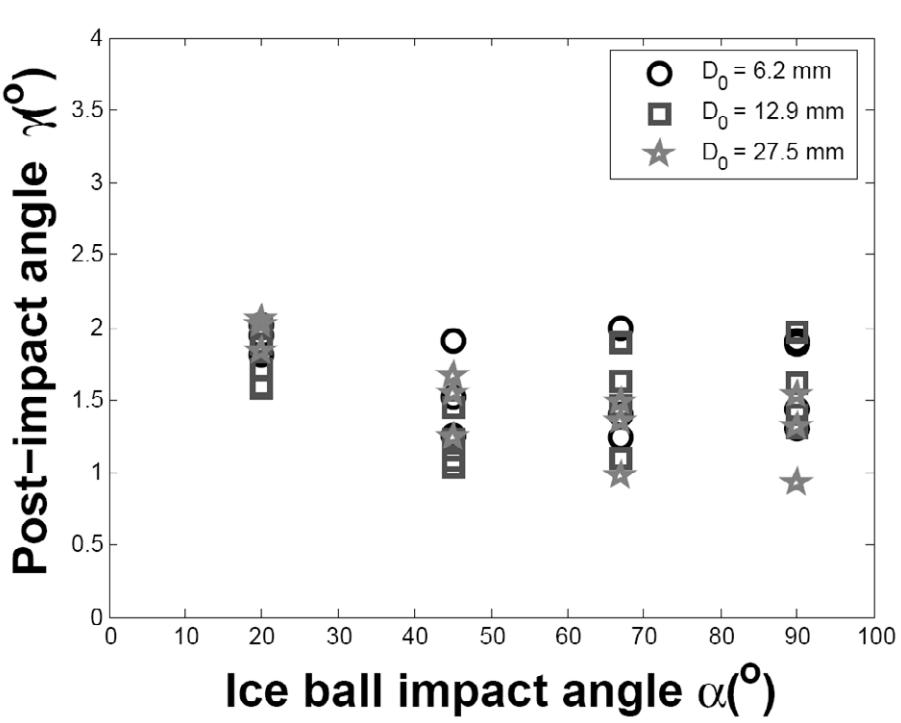

Figure 9: Values of the post-impact angle γ for the different experiments.

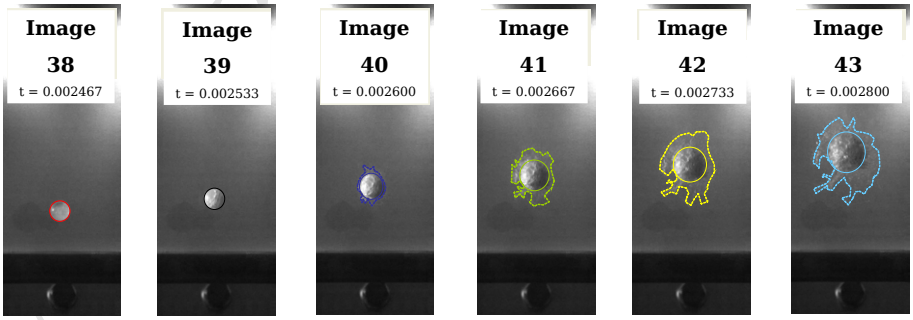

Figure 10: Analysis of images from the front camera: definition of the high density cloud contour (diameter: 12.9 mm, impact angle 20 °, impact velocity: 120.8 m.s^{-1}).

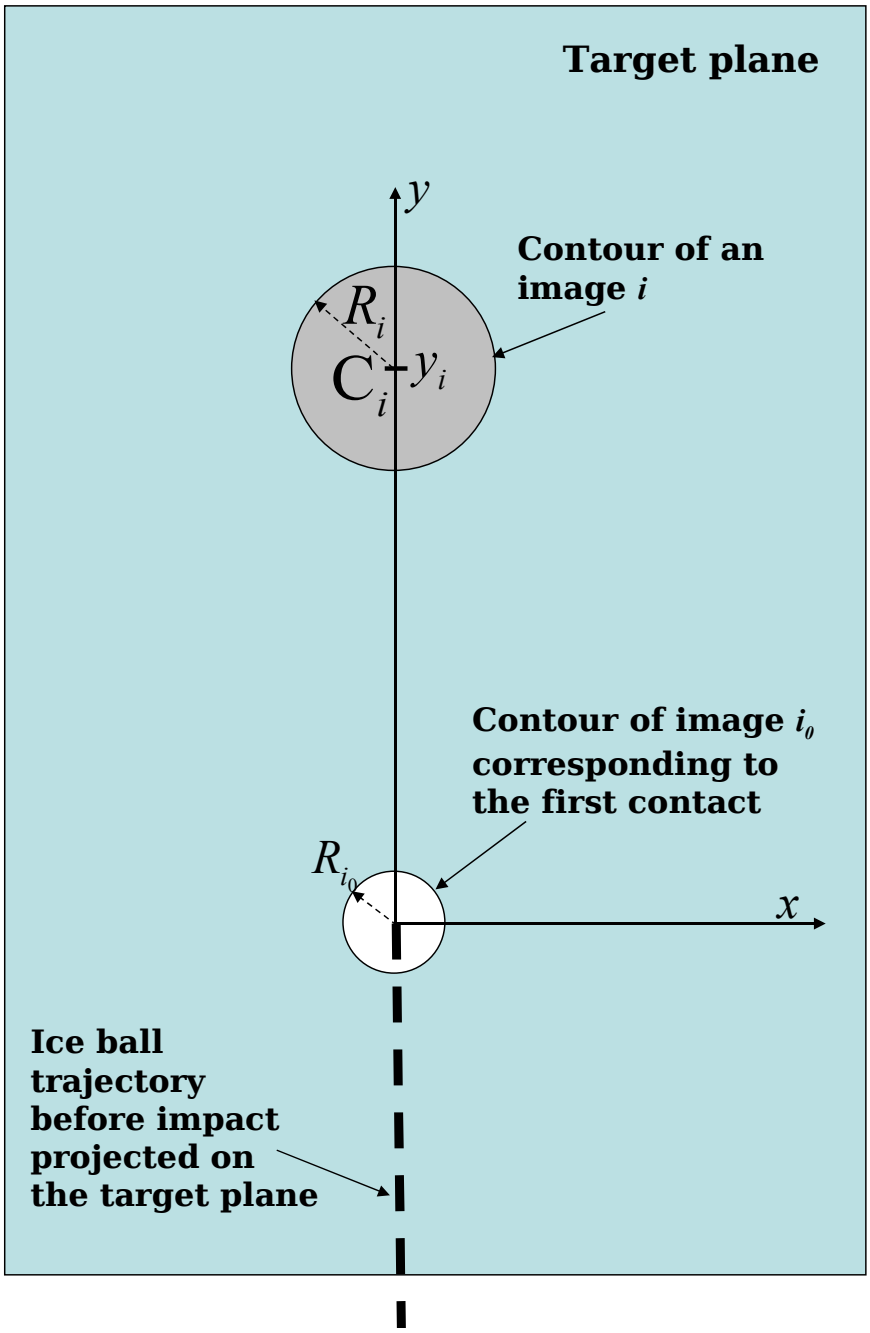

Figure 11: Shematic of the superposition of two circular contours on the image i_0 corresponding to the first (initial) contact and to a subsequent image i.

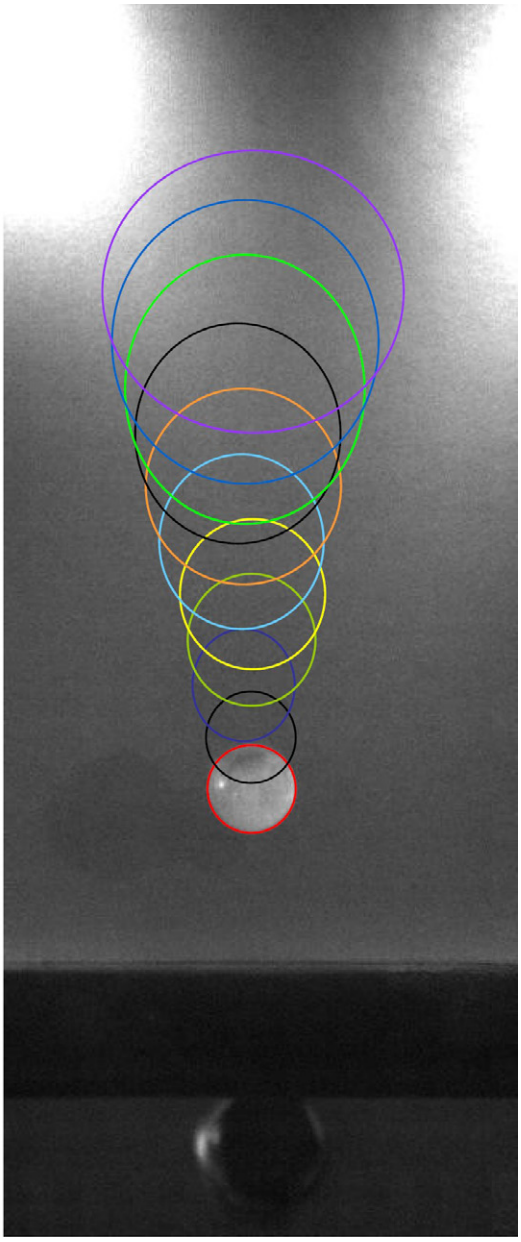

Figure 12: Superposition of circular contours: experimental result (diameter: 12.9 mm, impact angle 20 °, impact velocity: 120.8 m.s^{-1}).

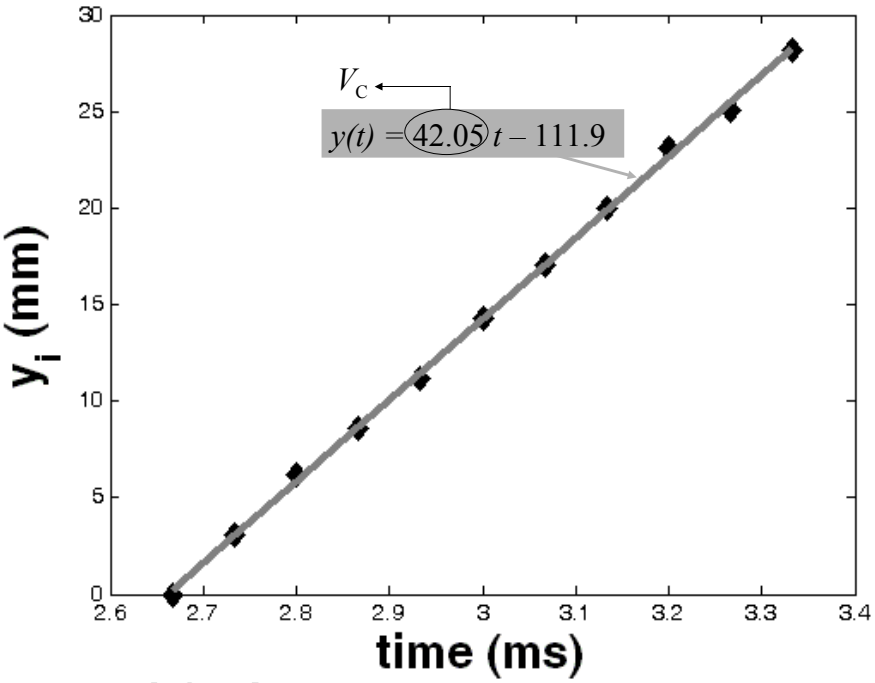

Figure 13: Evolution of the position of the cloud center with time (diameter: 12.9 mm, impact angle 67 °, impact velocity: 118.8 m.s^{-1}).

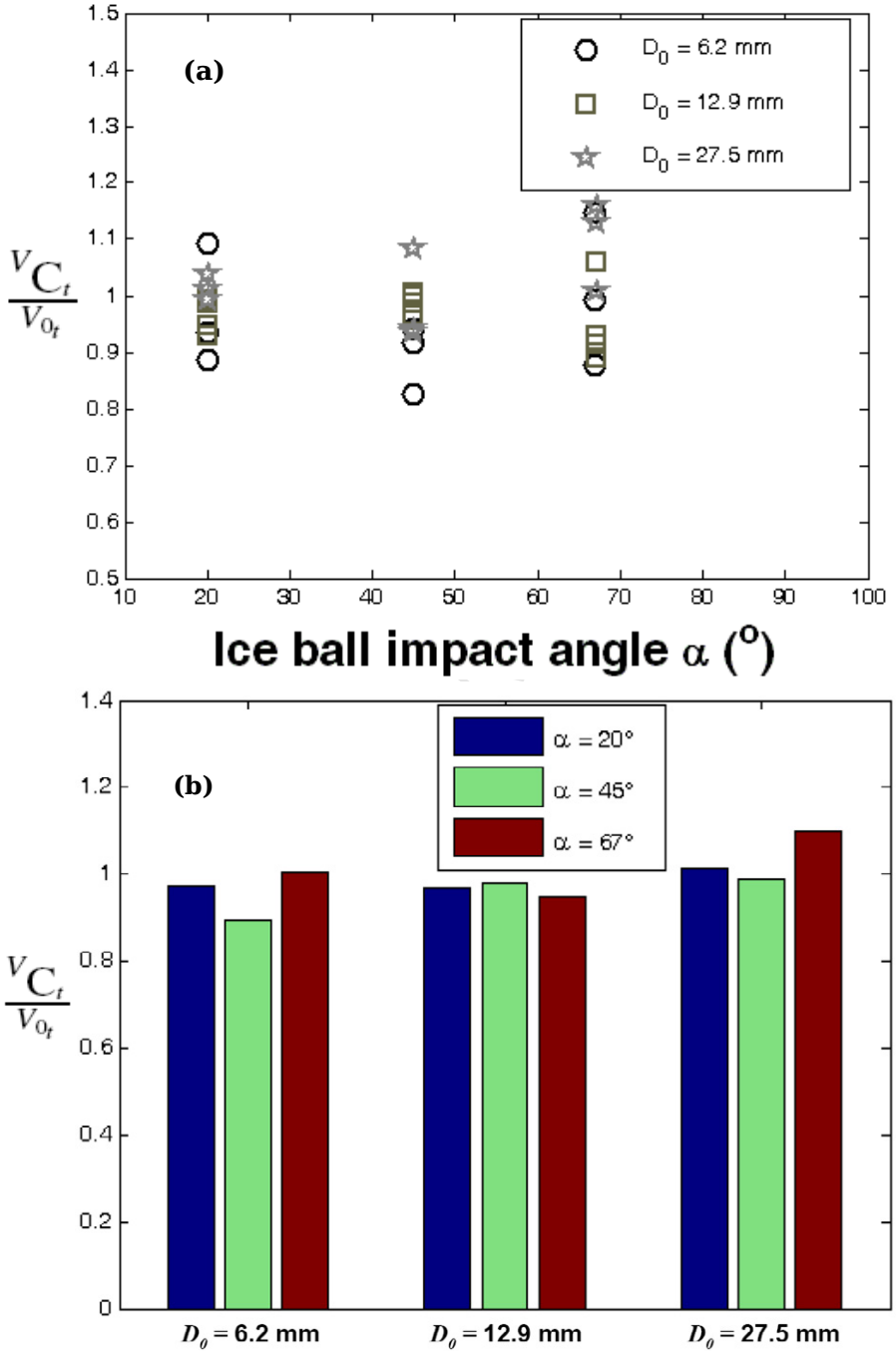

Figure 14: Values of the ratio V_{C_t}/V_{0_t}: (a) for all experiments; (b) average values for each configuration.

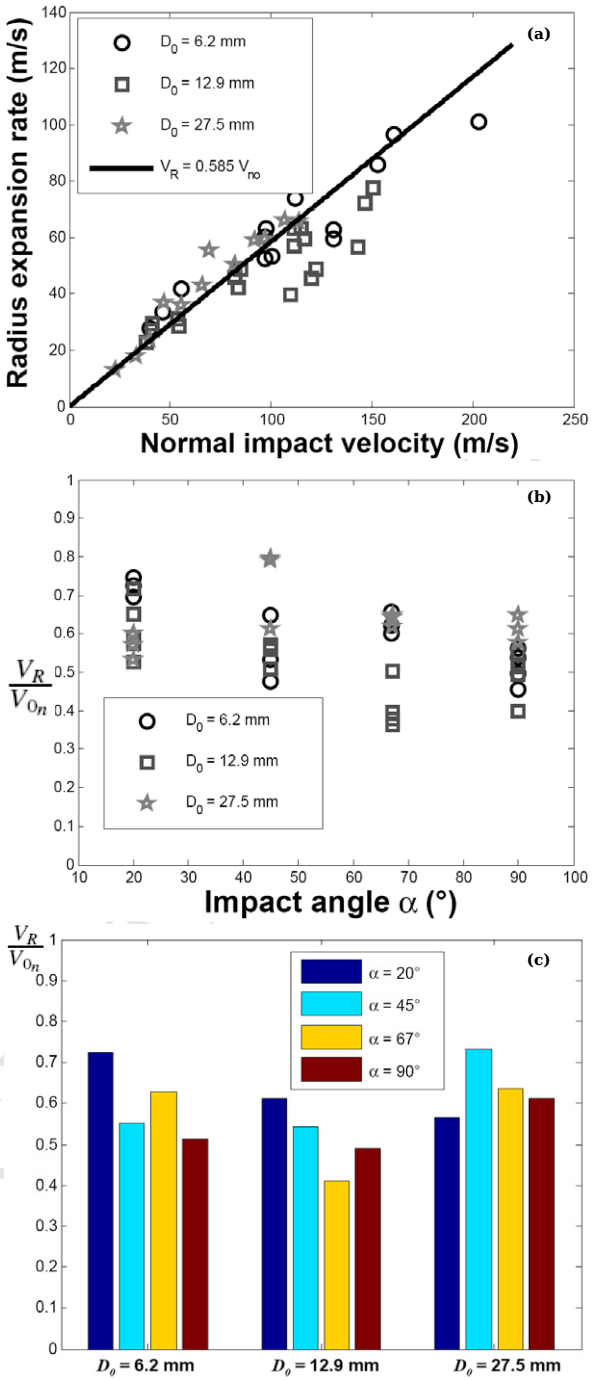

Figure 15: Radius expansion: (a) expansion rate V_R as a function of normal impact velocity V_{0_n}; (b) $K_n = V_R/V_{0_n}$ as a function of impact angle α and (c) averaged values of K_n.

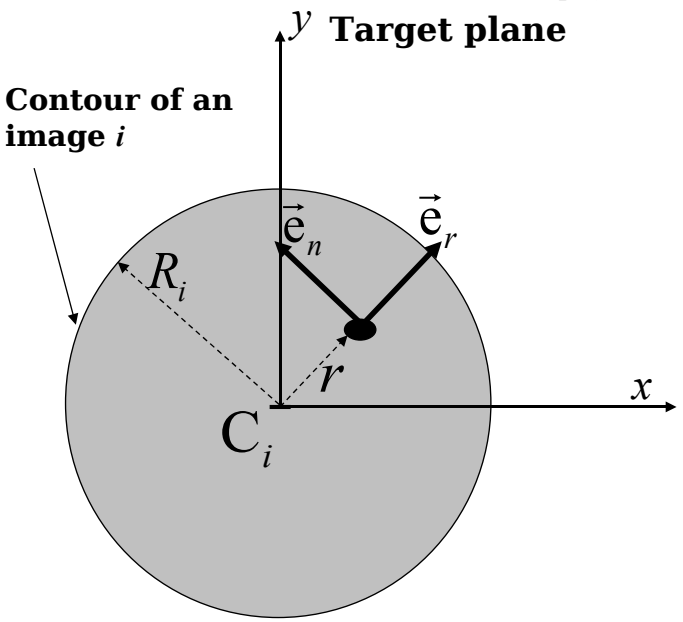

Figure 16: Mobile reference frame.

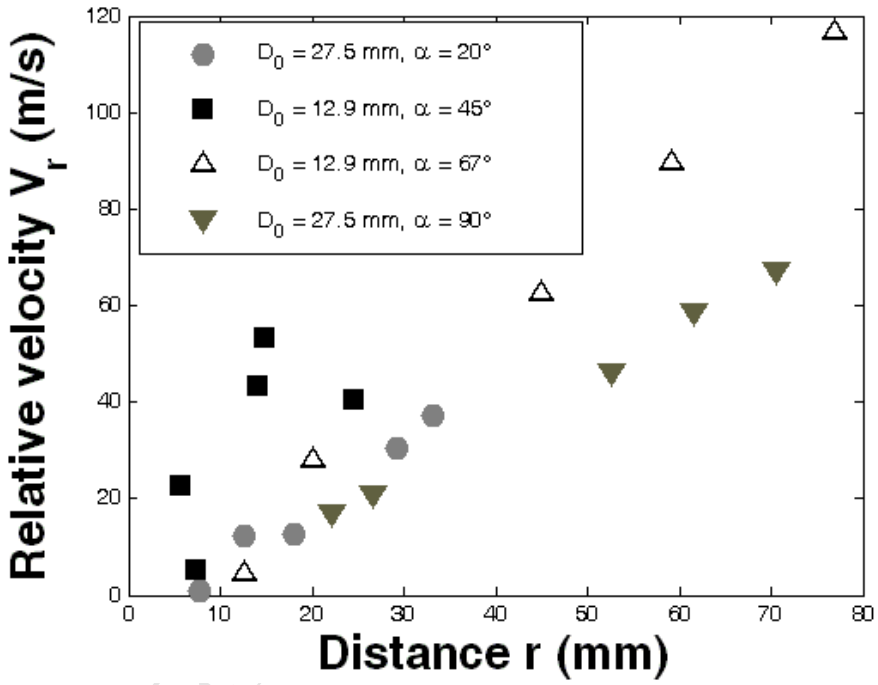

Figure 17: Relative velocity of fragments inside the cloud as a function of their distance to the cloud center.